Journal of Sound and Vibration 329 (2010) 5087–5104

Contents lists available at ScienceDirect

Journal of Sound and Vibration

journal homepage: www.elsevier.com/locate/jsvi

In-plane free vibration analysis of combined ring-beam structural systems by wave propagation

B. Chouvion *, C.H.J. Fox, S. McWilliam, A.A. Popov

Materials, Mechanics and Structures Division, Faculty of Engineering, University of Nottingham, University Park, Nottingham NG7 2RD, UK

ARTICLE INFO

Article history:
Received 23 October 2009
Received in revised form
28 April 2010
Accepted 22 May 2010
Handling Editor: S. Ilanko

ABSTRACT

This paper presents a systematic, wave propagation approach for the free vibration analysis of networks consisting of slender, straight and curved beam elements and complete rings. The analysis is based on a ray tracing method and a procedure to predict the natural frequencies and mode shapes of complex ring/beam networks is demonstrated. In the wave approach, the elements are coupled using reflection and transmission coefficients, and these are derived for discontinuities encountered in a MEMS rate sensor consisting of a ring supported on an array of folded beams. These are combined, taking into account wave propagation and decay, to provide a concise and efficient method for studying the free vibration problem. A simplification of the analysis that exploits cyclic symmetry in the structure is also presented. The effects of decaying near-field wave components are included in the formulation, ensuring that the solutions are exact. To illustrate the effectiveness of the approach, several numerical examples are presented. The predictions made using the proposed approach are shown to be in excellent agreement with a conventional FE analysis.

1. Introduction

Engineering structures often consist of a number of components that can be modelled as beams, curved bars and rings. Fig. 1 shows photographs and a schematic representation of a microelectromechanical systems (MEMS) ring-based rate sensor. The basic sensor structure is a resonator consisting of a slender circular ring supported on slender spokes as shown. Operation of the device makes use of Coriolis coupling between particular modes of vibration of the resonator to determine the rate of rotation about one or more axes [1]. The design and optimisation of structures like these is aided greatly by the availability of efficient techniques to rapidly determine the effects of variations in geometry and dimensions on vibration characteristics such as natural frequencies and mode shapes. The performance of MEMS sensors like the one shown in Fig. 1 is often highly dependent on the level of damping. One important damping mechanism is support loss or attachment loss [2,3], which accounts for the transmission of vibration from the resonator into the supporting structure. Sensors like the one shown in Fig. 1 were first designed and used to vibrate in-plane only. These represent the main motivation of the work reported in this paper, which deals with the development of an efficient approach to analyse the in-plane vibrations of ring/beam structures that has the potential to be used to predict support losses. Future publications will focus on predicting support losses in ring-resonators and on considering out-of-plane vibrations of combined ring/beam systems.

* Corresponding author.
E-mail address: eaxbc@nottingham.ac.uk (B. Chouvion).

0022-460X/$ - see front matter © 2010 Elsevier Ltd. All rights reserved.
doi:10.1016/j.jsv.2010.05.023

Nomenclature

$\mathbf{a}$	wave amplitude vector
A	cross-sectional area
$\mathbf{B}^{(j)}$	$[3\times3]$ reflection coefficients matrix at discontinuity j
d_j	diameter of the rigid joint
$\mathbf{D}$	diagonal dispersion matrix
E	modulus of elasticity
I	second moment of area
$\mathbf{I}$	identity matrix
I_j	inertia of the rigid joint
k	wavenumber
k_1, k_2, k_3	principal extensional, flexural and decaying wavenumbers
k_L	longitudinal wavenumber
k_F	flexural wavenumber
L, $L^{(j)}$	length, length of the (j)th portion
L_0	distance between two substructures, or length of one side of the regular polygon
m_j	mass of the rigid joint
M	bending moment
N	number of sectors in the cyclic symmetry simplification, number of point masses, number of sides in regular polygons
R	mean radius of curvature, distance centre/corner for regular polygons
$\mathbf{R}^{(j)}$	$[3\times3]$ reflection coefficients matrix at boundary j
s	circumferential coordinate along the curved beam or ring portion
S	shear force
t	time
T	tensile force
$\mathbf{T}$	transmission coefficients matrix
u	tangential, longitudinal displacement
$\hat{u}$	extensional wave amplitude
$\mathbf{u}$	wave amplitude row-vector containing three components: extensional, flexural and decaying waves
w	radial, flexural displacement
$\hat{w}$	flexural wave amplitude
x	coordinate along the beam centreline
X_j	amplitude ratio
α	angle
$\mathbf{\Delta}_{L^{(j)}}$	$[3\times3]$ dispersion matrix along the length $L^{(j)}$
κ	cyclic mode number
Λ	substructure name
$\mathbf{\Pi}^{(i)\to(j)}$	$[3\times3]$ transmission coefficients matrix from (i) to (j)
ρ	mass density
$\mathbf{\Upsilon}$	$[3\times3]$ change of phase matrix
ψ	rotational motion of the cross-section
ω	angular frequency

Subscripts

1, 2, 3	denotes the wave type (mainly extensional, flexural and decaying)
b	straight beam related
initial	first wave taken into account in the ray tracing approach
r	ring portion related

Superscripts

(l), (r)	left or right portion considered
(j)	index of the portion considered
T	matrix transpose
+	denotes positive-going direction in s or x-axis
−	denotes negative-going direction in s or x-axis

The vibrational response of simple structures such as uncoupled beams or rings can be determined without difficulty [4] using the Rayleigh–Ritz or modal approaches. However, the analysis of complex systems containing several elements is more challenging. A possible method is the dynamic stiffness method [5] that has been developed to analyse in-plane and out-of-plane vibrations of networks. Each component is modelled using an exact solution and matrices coupling

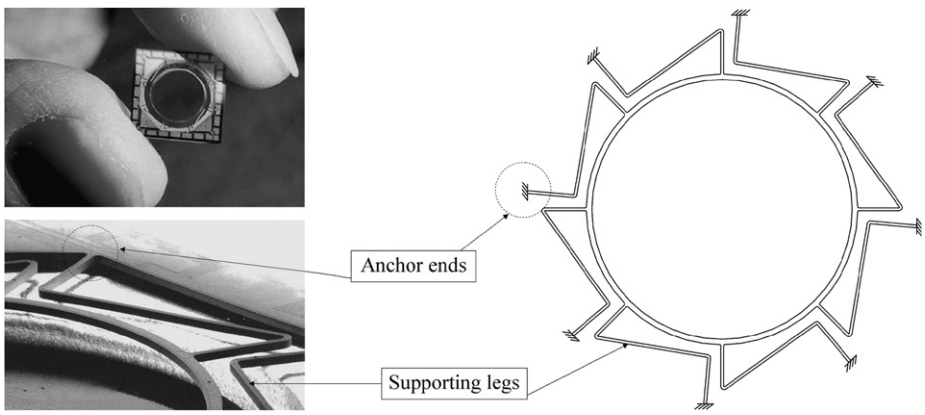

Fig. 1. Ring-based rate sensor and its leg shape.

displacements and forces of each element with its neighbours are considered. The Wittrick–Williams algorithm [6] is customarily applied to determine the natural frequencies of the system. The dynamic stiffness method and the Wittrick–Williams algorithm have previously been applied to curved members in [7] and have exploited cyclic symmetry of structures, e.g. see [8]. An alternative method is the use of finite element (FE) packages that are employed widely to model complex structures, and can be used to calculate natural frequencies and mode shapes, and the vibration response. However, it is often computationally expensive if many different FE meshes need to be generated when performing optimisation studies. In contrast, the wave-based approach considered in this paper not only allows natural frequencies and mode shapes to be determined efficiently as exact solutions, but its formulation also allows the geometry and size of the structure to be varied easily and efficiently. The dynamic stiffness method, which is also based on an exact analysis, could have been applied at this point but wave approaches have proved to be powerful for analysing the energy transmission through structural networks [9] and this characteristic will be used in future work to calculate support losses in MEMS structures.

The vibrations of elastic structures, such as strings, beams, and rings, can be described in terms of waves that propagate and decay in waveguides. Such waves are reflected and transmitted when incident upon discontinuities [10,11]. Mace [12,13] was one of the first to use a wave approach to determine the power flow between two coupled Euler–Bernoulli beams and the distribution of energy within the system. In his model, each subsystem was essentially one-dimensional, supporting just one wave type. Mace showed that when the coupling between the two beams is weak, peaks in coupling power occur near the natural frequencies of the uncoupled subsystems. Expanding the work of Mace, Langley [14] developed a ray tracing method to evaluate the response of one-dimensional structures subjected to harmonic excitation. Ashby [15] incorporated near-field effects and validated the method for a simply supported beam. A similar approach was used recently [16] to describe wave propagation, transmission and reflection in Timoshenko beams under various conditions. One of the earliest investigations of wave motion in curved beams was by Graff [10], who developed equations for a ring, accounting for extension, shear and rotary inertia. Dispersion curves were presented showing the effects of curvature, shear, and inertia on the wave propagation. Kang et al. [17] extended the ray tracing method to planar circular curved beam structures including the effects of attenuating wave components. As far as the authors are aware, the technique has not been used on complex structures such as the one presented in Fig. 1.

The principle behind the present approach is called phase closure [18] (also called wave-train closure [11]). This principle states that if the phase difference between incident and reflected waves is an integer multiple of 2π, then the waves propagate at a natural frequency and their motions constitute a vibration mode. The compact and systematic methodology of this approach allows complex structures, such as multi-span beams, trusses and aircraft panels with periodic supports to be analysed.

The application of the ray tracing method relies on having knowledge of the detailed propagation, reflection, and transmission characteristics of waves in different parts of the structure. In particular, the precise detail of the waves at discontinuities is needed to predict their reflection and transmission. The reflection and transmission of waves in Euler–Bernoulli beams at various discontinuities have been determined by Mace [19]. In the present paper, the method, still based on Euler–Bernoulli theory, has been extended to analyse the natural frequencies of a structure, such as that shown in Fig. 1, which contains more complex discontinuities, like those arising between a ring and a straight beam. The method has also been extended to take account of the cyclic symmetry properties of structures.

The manuscript is organised as follows. Sections 2 and 3 provide a brief review of the basics of wave propagation in beams and of the ray tracing method. Section 4 presents a derivation of the transmission coefficients for different discontinuities relevant to the structure of interest, while Section 5 deals with a simplification of the analysis for structures exhibiting cyclic symmetry. Section 6 presents numerical results, based on structures of varying complexity, including the ring-based rate sensor shown in Fig. 1. Section 7 gives a summary and a statement of conclusions.

2. Wave propagation in straight and curved beams

This section introduces the harmonic wave solution of the fundamental governing equations of in-plane motion of curved beams with constant radius, neglecting shear deformation and rotary inertia. The equations obtained are well known [10,17,20] and are used extensively in later sections.

In any curved beam section, the tangential and radial displacements can be expressed as a sum of waves travelling in the right and left directions [20], i.e.,

$$u = \sum_{i=1}^{3} \left(\hat{u}_i^{+} \mathrm{e}^{-\mathrm{i}k_i s} + \hat{u}_i^{-} \mathrm{e}^{\mathrm{i}k_i (s-L)} \right) \mathrm{e}^{\mathrm{i}\omega t}, \tag{1a}$$

$$w = \sum_{i=1}^{3} \left(\hat{w}_i^{+} \mathrm{e}^{-\mathrm{i}k_i s} + \hat{w}_i^{-} \mathrm{e}^{\mathrm{i}k_i (s-L)} \right) \mathrm{e}^{\mathrm{i}\omega t}. \tag{1b}$$

In these expressions, u and w are the tangential and radial displacements; $\hat{u}_i^{+}$ and $\hat{w}_i^{+}$ are the complex amplitudes of the tangential and radial waves travelling in the positive s direction; while $\hat{u}_i^{-}$ and $\hat{w}_i^{-}$ are the complex amplitudes of the tangential and radial waves travelling in the negative s direction; k_i is the complex wavenumber associated with the waves

of amplitude $\hat{u}_i^{\pm}$ and $\hat{w}_i^{\pm}$; and, ω is the angular frequency. A list of symbols is provided in the Nomenclature. The wavenumbers k_i (i=1, 2, 3) are obtained by solving the characteristic (dispersion) equation for curved beams [20]. When the mean radius R of the curved beam tends to infinity, the root which tends to k_L (k_L being the wavenumber of longitudinal waves in a straight beam) is related to predominantly longitudinal waves and is denoted by k_1; the roots which tend to k_F and $-ik_F$ (k_F being the wavenumber of flexural waves in a straight beam) are related to predominantly propagating far-field flexural waves and decaying near-field waves, respectively, and are denoted by k_2 and k_3, respectively. The waves travelling in the positive s direction ($\hat{u}_i^+$, $\hat{w}_i^+$) originate from the location s=0, whilst the waves travelling in the negative s direction ($\hat{u}_i^-$, $\hat{w}_i^-$) originate from the location s=L. In applications it is convenient to choose s=0 and L to be located at each end of the curved beam section.

From Eq. (1), it is clear that the radial and tangential displacements for a single curved section are defined by 12 unknown wave amplitudes. In general the amplitudes of these waves will depend on the waves travelling in other sections of the structure. However, for curved beams it can be shown that some of the radial and tangential wave amplitudes in a particular curved beam section are related to each other.

The ratio of the radial to tangential amplitudes of waves travelling in the same direction along a curved beam, having wavenumber k_i, is given by [20]

$$X_i = \frac{\hat{w}_i^+}{\hat{u}_i^+} = -\frac{\hat{w}_i^-}{\hat{u}_i^-} = -\frac{iERk_i(Ik_i^2+A)}{\rho R^2 A\omega^2-(EIR^2k_i^4+EA)}, \tag{2}$$

where A is the cross-sectional area of the curved beam, I is the second moment of area of the cross-section, E is Young's modulus, and ρ is the mass density. Non-zero values of this ratio show the coupling between radial and tangential waves. Thus for the wave amplitude pair ($\hat{u}_i^{\pm}$, $\hat{w}_i^{\pm}$) it is only necessary to determine one of the amplitudes, as the other is known implicitly from knowledge of the ratio X_i.

In any straight beam section, the equations governing the longitudinal and flexural displacements are uncoupled. The ratios expressed in Eq. (2) become X_1=0 and $X_2 = X_3 = \infty$. The longitudinal and flexural displacements in a straight beam can be described as the sum of waves purely propagating and purely decaying (near field) in the positive and negative directions, see [10] or for instance in Eq. (3).

For the curved beam or straight beam case, six independent unknown wave amplitudes are needed to determine the tangential (or longitudinal) and radial (or flexural) displacements: three in the positive s direction, and three in the negative s direction.

3. The ray tracing method

This section presents the development of the ray tracing method, which is an extension of the work carried out in [14]. It provides a systematic approach to the free vibration analysis of complex waveguide structures, and is used here to analyse coupled curved/straight beam structures such as the one presented in Fig. 1.

3.1. Simplified development for a two-beam example

To simplify the development and presentation, the case of a network composed of two straight beam components, coupled together at a discontinuity, and subjected to a harmonic vibration at frequency ω is considered, see Fig. 2. The analysis is performed for this simple case and can be extended easily to more complex cases (see Section 3.2).

The longitudinal u and flexural w displacements in any component of the structure are defined as a sum of waves, see Section 2. The displacements at a location having coordinate x in component (I) are expressed as

$$u(x,t) = \left(\hat{u}_1^{(\mathrm{I})+}e^{-ik_Lx} + \hat{u}_1^{(\mathrm{I})-}e^{ik_L(x-L^{(\mathrm{I})})}\right)e^{i\omega t}, \tag{3a}$$

$$w(x,t) = \left(\hat{w}_2^{(\mathrm{I})+}e^{-ik_Fx} + \hat{w}_3^{(\mathrm{I})+}e^{-k_Fx} + \hat{w}_2^{(\mathrm{I})-}e^{ik_F(x-L^{(\mathrm{I})})} + \hat{w}_3^{(\mathrm{I})-}e^{k_F(x-L^{(\mathrm{I})})}\right)e^{i\omega t}, \tag{3b}$$

where $L^{(\mathrm{I})}$ is the length of component (I), $\hat{u}_1^{(\mathrm{I})\pm}$, $\hat{w}_2^{(\mathrm{I})\pm}$ and $\hat{w}_3^{(\mathrm{I})\pm}$ are the amplitudes of the longitudinal, flexural propagating and decaying waves, respectively, in component (I). The amplitudes of waves travelling in the positive x direction

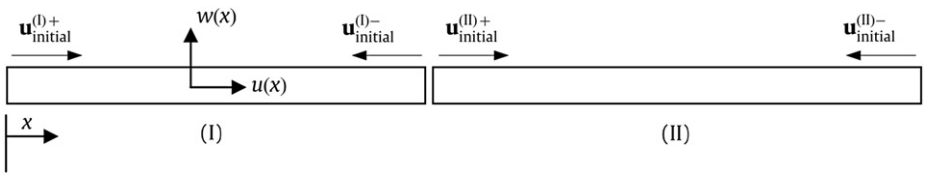

Fig. 2. Initial wave amplitudes considered for the ray tracing method in a two beam component system.

(with a superscript +) are defined at $x=0$, while the ones corresponding to waves travelling in the negative x direction (superscript $-$) are defined at $x=L^{(\mathrm{I})}$.

The ray tracing method considers an initial wave amplitude vector $\mathbf{a}_0$ which contains the initial waves amplitude sources in the 'positive' and 'negative' x direction for each beam, see Fig. 2. These waves start at any discontinuity and their amplitudes are maximum at the initial point. There are only non-zero terms in the excited beams. For the two-beam case considered, the initial wave amplitude vector has the form:

$$\mathbf{a}_{0_{[12\times1]}}=[\mathbf{u}^{(\mathrm{I})+}_{\mathrm{initial}}\ \ \mathbf{u}^{(\mathrm{I})-}_{\mathrm{initial}}\ \ \mathbf{u}^{(\mathrm{II})+}_{\mathrm{initial}}\ \ \mathbf{u}^{(\mathrm{II})-}_{\mathrm{initial}}]^{\mathrm{T}}. \tag{4}$$

Each $\mathbf{u}^{(j)\pm}_{\mathrm{initial}}$ represents the initial wave amplitude vector in component j ($j=\mathrm{I}, \mathrm{II}$). $\mathbf{u}^{(j)\pm}_{\mathrm{initial}}$ is a vector containing wave amplitudes corresponding to longitudinal, flexural and decaying waves and is defined as

$$\mathbf{u}^{(j)\pm}_{\mathrm{initial}}=[\hat{u}^{(j)\pm}_{1_{\mathrm{initial}}}\ \ \hat{w}^{(j)\pm}_{2_{\mathrm{initial}}}\ \ \hat{w}^{(j)\pm}_{3_{\mathrm{initial}}}]. \tag{5}$$

While the waves travel from one end of the component to the other end, the propagating waves change phase and the decaying waves change amplitude. These effects depend on the wavenumber k_i ($k_i=k_L$, k_F or $-\mathrm{i}k_F$) and the length $L^{(j)}$ of the component. The complex amplitude of the waves changes from $\hat{u}^{(j)\pm}_i$ to $\hat{u}^{(j)\pm}_i \mathrm{e}^{-\mathrm{i}k_iL^{(j)}}$. This phenomenon can be expressed using a diagonal matrix $\mathbf{D}$ called the dispersion matrix (or transfer matrix in [16]) whose diagonal elements have the form $\mathrm{D}_{ii}=\mathrm{e}^{-\mathrm{i}k_iL^{(j)}}$, where k_i is the wavenumber associated with wave i and $L^{(j)}$ is the corresponding beam length.

When a wave hits a discontinuity (boundary at the end of a component or discontinuity between two different elements), it can be either reflected back in the opposite direction or transmitted to another waveguide component. By considering the complex wave amplitude transmission and reflection coefficients, the amplitude of the waves leaving the discontinuity can be evaluated. This scattering at a discontinuity can be expressed in terms of a transmission matrix $\mathbf{T}$ of complex wave amplitude transmission/reflection coefficients, where $\hat{v}_i=\mathrm{T}_{ij}\hat{v}_j$ and T_{ij} is the transmission coefficient from a wave of amplitude $\hat{v}_j$ to a wave of amplitude $\hat{v}_i$.

The dispersion matrix has the form:

$$\mathbf{D}_{[12\times12]}=\begin{bmatrix}\boldsymbol{\Delta}_{L^{(\mathrm{I})}} & \mathbf{0} & \mathbf{0} & \mathbf{0}\\ \mathbf{0} & \boldsymbol{\Delta}_{L^{(\mathrm{I})}} & \mathbf{0} & \mathbf{0}\\ \mathbf{0} & \mathbf{0} & \boldsymbol{\Delta}_{L^{(\mathrm{II})}} & \mathbf{0}\\ \mathbf{0} & \mathbf{0} & \mathbf{0} & \boldsymbol{\Delta}_{L^{(\mathrm{II})}}\end{bmatrix}, \tag{6}$$

where

$$\boldsymbol{\Delta}_{L^{(j)}[3\times3]}=\begin{bmatrix}\mathrm{e}^{-\mathrm{i}k_LL^{(j)}} & 0 & 0\\ 0 & \mathrm{e}^{-\mathrm{i}k_FL^{(j)}} & 0\\ 0 & 0 & \mathrm{e}^{-k_FL^{(j)}}\end{bmatrix},\quad j=\mathrm{I},\mathrm{II}.$$

The transmission matrix has the form:

$$\mathbf{T}_{[12\times12]}=\begin{bmatrix}\mathbf{0} & \mathbf{R}^{(\mathrm{I})} & \mathbf{0} & \mathbf{0}\\ \mathbf{B}^{(\mathrm{I})} & \mathbf{0} & \mathbf{0} & \boldsymbol{\Pi}^{(\mathrm{II})\to(\mathrm{I})}\\ \boldsymbol{\Pi}^{(\mathrm{I})\to(\mathrm{II})} & \mathbf{0} & \mathbf{0} & \mathbf{B}^{(\mathrm{II})}\\ \mathbf{0} & \mathbf{0} & \mathbf{R}^{(\mathrm{II})} & \mathbf{0}\end{bmatrix}, \tag{7}$$

where $\mathbf{R}^{(\mathrm{I})}_{[3\times3]}$ and $\mathbf{R}^{(\mathrm{II})}_{[3\times3]}$ contain the reflection coefficients at the boundaries in beams (I) and (II) respectively; $\mathbf{B}^{(\mathrm{I})}_{[3\times3]}$ and $\mathbf{B}^{(\mathrm{II})}_{[3\times3]}$ contain the reflection coefficients at the discontinuity between beams (I) and (II), respectively; $\boldsymbol{\Pi}^{(i)\to(j)}_{[3\times3]}$ contains the transmission coefficients from waves incident in beams (i) to (j).

After the waves have traversed along the length of the beam and one transmission has taken place, the new wave amplitude vector $\mathbf{a}_1$ can be written as

$$\mathbf{a}_1=\mathbf{TD}\mathbf{a}_0. \tag{8}$$

This vector contains the wave amplitudes after one ray trace. This approach can be repeated to give the wave amplitudes after the next ray trace: $\mathbf{a}_2=\mathbf{TD}\mathbf{a}_1=(\mathbf{TD})^2\mathbf{a}_0$. The cycle of decay, propagation and transmission can be continued indefinitely. After an infinite number of ray traces, the total set of wave amplitudes $\mathbf{a}$ present in the structure is expressed as the sum of all the previous waves:

$$\mathbf{a}=\mathbf{a}_0+\mathbf{a}_1+\mathbf{a}_2+\cdots+\mathbf{a}_\infty=\sum_{i=0}^{\infty}(\mathbf{TD})^i\mathbf{a}_0. \tag{9}$$

Eq. (9) is a geometric series with common ratio $\mathbf{TD}$ and first term $\mathbf{a}_0$. As $|\mathbf{TD}|<1$, meaning that the amplitudes of the waves are attenuated from one trace to the next, it can be derived from Eq. (9) that the final set of wave amplitudes $\mathbf{a}$ is governed by

$$(\mathbf{I}-\mathbf{TD})\mathbf{a}=\mathbf{a}_0, \tag{10}$$

where **I** is the identity matrix. In Eq. (10), the term **a** represents the final set of wave amplitudes and defines the motion at any point in the system.

For the free vibration case, the initial wave amplitude vector is zero, and Eq. (10) becomes

$$(\mathbf{I}-\mathbf{TD})\mathbf{a}=\mathbf{0}. \tag{11}$$

Non-trivial solutions to this equation occur when

$$|\mathbf{I}-\mathbf{TD}|=0. \tag{12}$$

This is the characteristic equation from which the natural frequencies of the system can be found. This equation can be solved analytically for systems such as a simple beam with clamped, free or pinned boundary conditions or for a perfect ring (see Section 6.1). For more complex structures, a numerical solution is required.

The corresponding mode shape can be determined by back-substituting the frequency solutions ω_n in the **T** and **D** matrices, which are both frequency dependent, and calculating the corresponding wave amplitude vector **a** that is the solution to Eq. (11). These wave amplitudes can be used in Eq. (3) to determine the displacement mode shape.

For forced response analysis, an external force or moment has the effect of injecting waves into the structure, e.g. see [16]. This would be considered into the $\mathbf{a}_0$ term with non-zero terms in the excited beams. Solving Eq. (10) can then lead to the steady-state response.

3.2. Development of a more a complex example

The ray tracing method was presented above for a simple two-beam system, but can be extended easily to a more complex structure. Here it is applied to the ring-based rate sensor shown in Fig. 1. In this example, the supporting legs consist of straight beams connected at different angles.

For simplification, the ray tracing method is applied here to only a single ring portion containing a single supporting leg. The set of initial wave amplitudes considered are presented in Fig. 3. The system is divided into five different components: two ring portions (one on either side of the discontinuity ring/leg) and three straight beams. The initial wave amplitude vector is defined as

$$\mathbf{a}_{0_{[30\times1]}}=[\mathbf{u}^{(\mathrm{I})+}_{\mathrm{initial}}\ \mathbf{u}^{(\mathrm{I})-}_{\mathrm{initial}}\ \mathbf{u}^{(\mathrm{II})+}_{\mathrm{initial}}\ \mathbf{u}^{(\mathrm{II})-}_{\mathrm{initial}}\ \cdots\ \cdots\ \mathbf{u}^{(\mathrm{V})+}_{\mathrm{initial}}\ \mathbf{u}^{(\mathrm{V})-}_{\mathrm{initial}}]^{\mathrm{T}}, \tag{13}$$

where $\mathbf{u}^{(j)\pm}_{\mathrm{initial}}=[\hat{u}1^{(j)\pm}_{\mathrm{initial}}\ \hat{w}2^{(j)\pm}_{\mathrm{initial}}\ \hat{w}3^{(j)\pm}_{\mathrm{initial}}]$. Waves start at all discontinuities and in each direction. Their amplitude is taken to be maximum at their initial point. Eq. (1) would imply the $\mathbf{u}^{(j)\pm}_{\mathrm{initial}}$ vector to be of order six for the curved members; however, only three of these amplitudes are independent due to using the X_i ratio of Eq. (2). In this example, $\mathbf{u}^{(\mathrm{I})+}_{\mathrm{initial}}$ and $\mathbf{u}^{(\mathrm{II})-}_{\mathrm{initial}}$ are evaluated at the joint with the neighbouring legs. The wavenumbers k_1, k_2 and k_3 (see Section 2) are associated with the amplitudes $\hat{u}^{(j)\pm}_1$, $\hat{w}^{(j)\pm}_2$ and $\hat{w}^{(j)\pm}_3$, respectively.

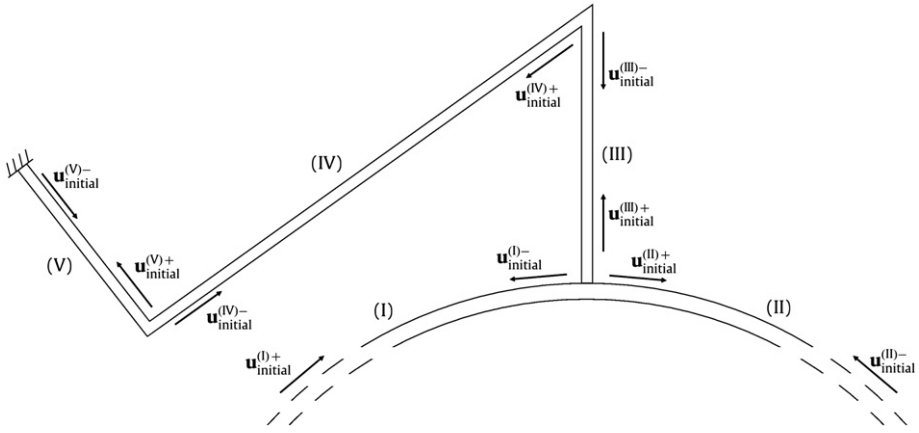

Fig. 3. Initial wave amplitudes considered for the ray tracing method in one sector of the ring-based rate sensor.

The transmission and dispersion matrices corresponding to Fig. 3, with wave amplitude vector **a**, defined in Eq. (13), are as follows:

$$\mathbf{T}_{[30\times30]}=\begin{bmatrix}
\mathbf{0} & \mathbf{R}^{(\mathrm{I})} & \mathbf{0} & \mathbf{0} & \mathbf{0} & \mathbf{0} & \mathbf{0} & \mathbf{0} & \mathbf{0} & \mathbf{0}\\
\mathbf{B}^{(\mathrm{I})+} & \mathbf{0} & \mathbf{0} & \boldsymbol{\Pi}^{(\mathrm{II})\to(\mathrm{I})} & \mathbf{0} & \boldsymbol{\Pi}^{(\mathrm{III})\to(\mathrm{I})} & \mathbf{0} & \mathbf{0} & \mathbf{0} & \mathbf{0}\\
\boldsymbol{\Pi}^{(\mathrm{I})\to(\mathrm{II})} & \mathbf{0} & \mathbf{0} & \mathbf{B}^{(\mathrm{II})-} & \mathbf{0} & \boldsymbol{\Pi}^{(\mathrm{III})\to(\mathrm{II})} & \mathbf{0} & \mathbf{0} & \mathbf{0} & \mathbf{0}\\
\mathbf{0} & \mathbf{0} & \mathbf{R}^{(\mathrm{II})} & \mathbf{0} & \mathbf{0} & \mathbf{0} & \mathbf{0} & \mathbf{0} & \mathbf{0} & \mathbf{0}\\
\boldsymbol{\Pi}^{(\mathrm{I})\to(\mathrm{III})} & \mathbf{0} & \mathbf{0} & \boldsymbol{\Pi}^{(\mathrm{II})\to(\mathrm{III})} & \mathbf{0} & \mathbf{B}^{(\mathrm{III})-} & \mathbf{0} & \mathbf{0} & \mathbf{0} & \mathbf{0}\\
\mathbf{0} & \mathbf{0} & \mathbf{0} & \mathbf{0} & \mathbf{B}^{(\mathrm{III})+} & \mathbf{0} & \mathbf{0} & \boldsymbol{\Pi}^{(\mathrm{IV})\to(\mathrm{III})} & \mathbf{0} & \mathbf{0}\\
\mathbf{0} & \mathbf{0} & \mathbf{0} & \mathbf{0} & \boldsymbol{\Pi}^{(\mathrm{III})\to(\mathrm{IV})} & \mathbf{0} & \mathbf{0} & \mathbf{B}^{(\mathrm{IV})-} & \mathbf{0} & \mathbf{0}\\
\mathbf{0} & \mathbf{0} & \mathbf{0} & \mathbf{0} & \mathbf{0} & \mathbf{0} & \mathbf{B}^{(\mathrm{IV})+} & \mathbf{0} & \mathbf{0} & \boldsymbol{\Pi}^{(\mathrm{V})\to(\mathrm{IV})}\\
\mathbf{0} & \mathbf{0} & \mathbf{0} & \mathbf{0} & \mathbf{0} & \mathbf{0} & \boldsymbol{\Pi}^{(\mathrm{IV})\to(\mathrm{V})} & \mathbf{0} & \mathbf{0} & \mathbf{B}^{(\mathrm{V})-}\\
\mathbf{0} & \mathbf{0} & \mathbf{0} & \mathbf{0} & \mathbf{0} & \mathbf{0} & \mathbf{0} & \mathbf{0} & \mathbf{R}^{(\mathrm{V})} & \mathbf{0}
\end{bmatrix}, \tag{14}$$

$$\mathbf{D}_{[30\times30]}=\begin{bmatrix}
\boldsymbol{\Delta}_{L^{(\mathrm{I})}} & \mathbf{0} & \mathbf{0} & \mathbf{0} & \dots & \mathbf{0} & \mathbf{0}\\
\mathbf{0} & \boldsymbol{\Delta}_{L^{(\mathrm{I})}} & \mathbf{0} & \mathbf{0} & \dots & \mathbf{0} & \mathbf{0}\\
\mathbf{0} & \mathbf{0} & \boldsymbol{\Delta}_{L^{(\mathrm{II})}} & \mathbf{0} & \dots & \mathbf{0} & \mathbf{0}\\
\mathbf{0} & \mathbf{0} & \mathbf{0} & \boldsymbol{\Delta}_{L^{(\mathrm{II})}} & \dots & \mathbf{0} & \mathbf{0}\\
\vdots & \vdots & \vdots & \vdots & \ddots & \vdots & \vdots\\
\mathbf{0} & \mathbf{0} & \mathbf{0} & \mathbf{0} & \dots & \boldsymbol{\Delta}_{L^{(\mathrm{V})}} & \mathbf{0}\\
\mathbf{0} & \mathbf{0} & \mathbf{0} & \mathbf{0} & \dots & \mathbf{0} & \boldsymbol{\Delta}_{L^{(\mathrm{V})}}
\end{bmatrix}. \tag{15}$$

All matrix entities present in **T** and **D** are $[3\times3]$ matrices. The matrices $\mathbf{R}^{(j)}$ (j=I, II, V) contain the reflection coefficients at the boundaries. The boundaries in components (I) and (II) are not 'real' boundaries in the ring-based rate sensor. They have been introduced here to demonstrate how the **T** matrix is formed. The wave amplitudes $\mathbf{u}^{(\mathrm{I})+}$ and $\mathbf{u}^{(\mathrm{II})-}$ are functions of the waves incident from the neighbouring legs and ring portions. The matrices $\mathbf{B}^{(j)+}$ and $\mathbf{B}^{(j)-}$ contain the reflection coefficients at the discontinuity situated at the positive or negative end of component (j). The matrices $\boldsymbol{\Pi}^{(i)\to(j)}$ contain the transmission coefficient from waves incident from components (i) to (j). The $\boldsymbol{\Delta}_{L^{(j)}}$ matrices are defined as

$$\boldsymbol{\Delta}_{L^{(j)}}=\begin{bmatrix}
\mathrm{e}^{-\mathrm{i}k_1L^{(j)}} & 0 & 0\\
0 & \mathrm{e}^{-\mathrm{i}k_2L^{(j)}} & 0\\
0 & 0 & \mathrm{e}^{-\mathrm{i}k_3L^{(j)}}
\end{bmatrix}. \tag{16}$$

For the straight beam sections (III), (IV) and (V), $k_1=k_L$, $k_2=k_F$ and $k_3=-\mathrm{i}k_F$. The analysis performed is similar to the simple case considered in Section 3.1. However, the matrices involved are much larger.

The transmission coefficients for discontinuities such as the ones encountered in the ring-based rate sensor are derived in Section 4. In a complex structure where the same discontinuity is encountered several times, the transmission coefficients only need to be calculated once. These coefficients will then be placed in the overall **T** matrix containing all transmission coefficients of the system. For example, for the entire ring-based rate sensor studied later, the overall matrices involved in the ray tracing method (**T** and **D**) have a size of $[192\times192]$. But there are no more transmission coefficients needed than the ones presented in Eq. (14). By solving Eq. (12), the natural frequencies of the system can be calculated.

As seen in this section, the ray tracing method requires several transmission coefficients matrices, and these are considered next.

4. Transmission coefficients

Transmission coefficients are calculated by considering the continuity and force equilibrium equations at discontinuities taken in isolation from the rest of the structure. This section presents a derivation of the principal transmission coefficients encountered in the MEMS sensor analysed later. This includes transmission through connected beams, and transmission between a ring and an attached beam. The well-known reflection coefficients of waves in a straight beam at common boundaries such as clamped, free or pinned ends were derived in [10,11].

4.1. Ring/beam transmission

The general case for the transmission between a ring and an attached beam is investigated first. The configuration considered is shown in Fig. 4. The beam forms an angle α with the ring. The discontinuity is modelled as a rigid joint (cylindrical mass) connecting two ring portions and a beam. This joint has been introduced to study the influence on the transmission coefficients of an added mass or inertia at the discontinuity. This analysis is an extension of the work carried out in [15] that studied the energy transmission between straight beams.

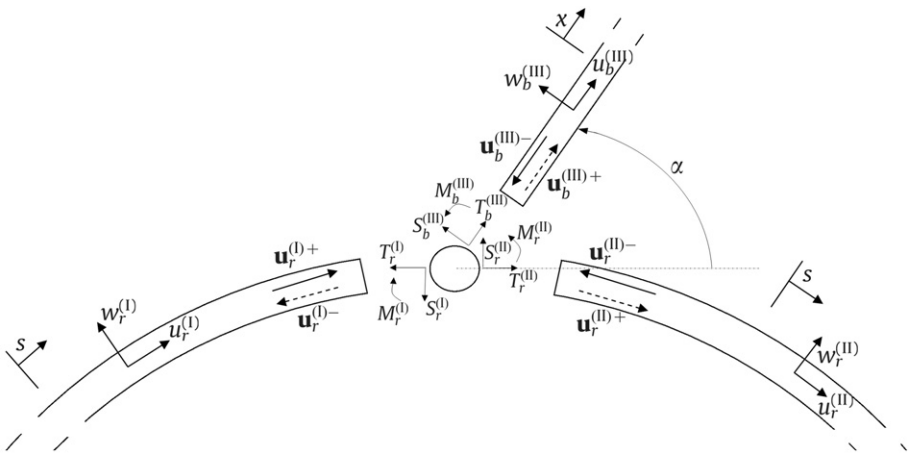

Fig. 4. Transmission between a ring and an attached beam.

In Fig. 4, the subscripts r and b relate to the ring and the beam respectively, the superscript (j) (j=I, II, III) corresponds to the component considered (two ring parts and one beam part), the superscript k (k=+, −) corresponds to the direction of propagation of the waves (positive and negative direction, respectively). Each of the variables $\mathbf{u}_r^{(I)+}$, $\mathbf{u}_r^{(I)-}$, $\mathbf{u}_r^{(II)+}$, $\mathbf{u}_r^{(II)-}$, $\mathbf{u}_b^{(III)+}$ and $\mathbf{u}_b^{(III)-}$ represents a set of wave amplitudes consisting of a principal extensional wave, a principal flexural propagating wave, and a principal decaying wave:

$$\mathbf{u}_{r,b}^{(j)\pm} = [\hat{u}_1^{(j)\pm} \quad \hat{w}_2^{(j)\pm} \quad \hat{w}_3^{(j)\pm}]. \tag{17}$$

In addition, the waves represented by a plain arrow in Fig. 4 relate to waves incident on the discontinuity, while the dashed arrows are transmitted or reflected waves.

To obtain a general method, the wave incident on the joint along a portion, which can be a straight beam or a circular bar, is assumed to be either predominantly flexural, longitudinal or decaying in nature. The presence of the joint ensures that part of this wave is reflected back along the same portion and the remainder is transmitted into the other portions. This partial reflection is also accompanied by mode conversion, so that the incident wave can generate flexural, longitudinal and decaying wave components in each of the three portions.

Assembly of the equilibrium and continuity expressions at the joint yields a system of simultaneous equations that can be solved to provide values for the required transmission coefficients for each wave type. The transmission matrix $\mathbf{T}_{\text{ring/beam}}$ contains the transmission coefficients from any wave type, in any portion to any resulting wave after transmission or reflection. For example, in the case presented in Fig. 4, the equilibrium and continuity equations can be derived as follows. By suppressing the temporal terms in the wave solutions expressed in Section 2, the transverse displacements $w_r^{(I)}$, $w_r^{(II)}$ and $w_b^{(III)}$; the tangential displacements $u_r^{(I)}$, $u_r^{(II)}$ and $u_b^{(III)}$; and the rotations of a cross-section $\psi_r^{(I)}$, $\psi_r^{(II)}$ and $\psi_b^{(III)}$ at the ring portion (I) (left), the ring portion (II) (right) and the beam portion (III), respectively, can be expressed in terms of wave amplitudes.

By considering input waves coming from the three portion simultaneously, the displacements and slopes involved in each portion are:

Ring portions (j) (j=I, II):

$$u_r^{(j)}(s) = \hat{u}_1^{(j)+}\mathrm{e}^{-\mathrm{i}k_1 s} + \frac{1}{X_2}\hat{w}_2^{(j)+}\mathrm{e}^{-\mathrm{i}k_2 s} + \frac{1}{X_3}\hat{w}_3^{(j)+}\mathrm{e}^{-\mathrm{i}k_3 s} + \hat{u}_1^{(j)-}\mathrm{e}^{\mathrm{i}k_1 s} - \frac{1}{X_2}\hat{w}_2^{(j)-}\mathrm{e}^{\mathrm{i}k_2 s} - \frac{1}{X_3}\hat{w}_3^{(j)-}\mathrm{e}^{\mathrm{i}k_3 s}, \tag{18}$$

$$w_r^{(j)}(s) = X_1\hat{u}_1^{(j)+}\mathrm{e}^{-\mathrm{i}k_1 s} + \hat{w}_2^{(j)+}\mathrm{e}^{-\mathrm{i}k_2 s} + \hat{w}_3^{(j)+}\mathrm{e}^{-\mathrm{i}k_3 s} - X_1\hat{u}_1^{(j)-}\mathrm{e}^{\mathrm{i}k_1 s} + \hat{w}_2^{(j)-}\mathrm{e}^{\mathrm{i}k_2 s} + \hat{w}_3^{(j)-}\mathrm{e}^{\mathrm{i}k_3 s}, \tag{19}$$

$$\psi_r^{(j)}(s) = \frac{\partial w_r^{(j)}(s)}{\partial s} - \frac{u_r^{(j)}(s)}{R}. \tag{20}$$

Beam portion (III):

$$u_b^{(III)}(x) = \hat{u}_1^{(III)+}\mathrm{e}^{-\mathrm{i}k_L x} + \hat{u}_1^{(III)-}\mathrm{e}^{\mathrm{i}k_L x}, \tag{21}$$

$$w_b^{(III)}(x) = \hat{w}_2^{(III)+}\mathrm{e}^{-\mathrm{i}k_F x} + \hat{w}_3^{(III)+}\mathrm{e}^{-k_F x} + \hat{w}_2^{(III)-}\mathrm{e}^{\mathrm{i}k_F x} + \hat{w}_3^{(III)-}\mathrm{e}^{k_F x}, \tag{22}$$

$$\psi_b^{(III)}(x) = \frac{\partial w_b^{(III)}(x)}{\partial x}. \tag{23}$$

Assuming that the joint is located at s=0 (or x=0), displacement and slope continuity ensures that

$$u_r^{(\mathrm{I})} = u_r^{(\mathrm{II})}, \tag{24}$$

$$w_r^{(\mathrm{I})} = w_r^{(\mathrm{II})} - d_j \psi_r^{(\mathrm{II})}, \tag{25}$$

$$\psi_r^{(\mathrm{I})} = \psi_r^{(\mathrm{II})}, \tag{26}$$

$$u_r^{(\mathrm{I})} = u_b^{(\mathrm{III})}\cos\alpha - \left(w_b^{(\mathrm{III})} - \frac{d_j}{2}\psi_b^{(\mathrm{III})}\right)\sin\alpha, \tag{27}$$

$$w_r^{(\mathrm{I})} + \frac{d_j}{2}\psi_r^{(\mathrm{I})} = u_b^{(\mathrm{III})}\sin\alpha + \left(w_b^{(\mathrm{III})} - \frac{d_j}{2}\psi_b^{(\mathrm{III})}\right)\cos\alpha, \tag{28}$$

$$\psi_r^{(\mathrm{I})} = \psi_b^{(\mathrm{III})}, \tag{29}$$

where d_j is the diameter of the cylindrical rigid joint. The tensile forces $T_r^{(\mathrm{I})}$, $T_r^{(\mathrm{II})}$ and $T_b^{(\mathrm{III})}$; shear forces $S_r^{(\mathrm{I})}$, $S_r^{(\mathrm{II})}$ and $S_b^{(\mathrm{III})}$; bending moments $M_r^{(\mathrm{I})}$, $M_r^{(\mathrm{II})}$ and $M_b^{(\mathrm{III})}$ of the ring portion (I) (left), the ring portion (II) (right) and the beam portion (III), respectively, evaluated at the joint at s=0 (or x=0) are related by the equations:

$$-T_r^{(\mathrm{I})} + T_r^{(\mathrm{II})} + T_b^{(\mathrm{III})}\cos\alpha - S_b^{(\mathrm{III})}\sin\alpha = m_j\frac{\partial^2}{\partial t^2}u_r^{(\mathrm{I})}, \tag{30}$$

$$-S_r^{(\mathrm{I})} + S_r^{(\mathrm{II})} + T_b^{(\mathrm{III})}\sin\alpha + S_b^{(\mathrm{III})}\cos\alpha = m_j\frac{\partial^2}{\partial t^2}\left(w_r^{(\mathrm{I})} + \frac{d_j}{2}\psi_r^{(\mathrm{I})}\right), \tag{31}$$

$$-M_r^{(\mathrm{I})} + M_r^{(\mathrm{II})} + M_b^{(\mathrm{III})} + \frac{d_j}{2}(S_r^{(\mathrm{I})} + S_r^{(\mathrm{II})} + S_b^{(\mathrm{III})}) = I_j\frac{\partial^2}{\partial t^2}\psi_r^{(\mathrm{I})}, \tag{32}$$

where m_j and I_j are the mass and moment of inertia of the rigid joint. Forces and moments of the straight and curved beam sections are then expressed in terms of the displacements using the well-known force–displacement relationships, see e.g. [4]. The transmission coefficients $\hat{u}_j/\hat{u}_i$ from an incident wave $\hat{u}_i$ to a reflected or transmitted wave $\hat{u}_j$ ($\hat{u}_1^{(\mathrm{I})-}/\hat{u}_1^{(\mathrm{I})+}$, $\hat{w}_2^{(\mathrm{I})-}/\hat{u}_1^{(\mathrm{I})+}$, $\hat{w}_3^{(\mathrm{I})-}/\hat{u}_1^{(\mathrm{I})+}$, etc.) can be obtained by solving the above equations. Considering incident waves from all three portions and solving the resulting $[9\times 9]$ system of equations gives a $[9\times 9]$ matrix $\mathbf{T}_{\mathrm{ring/beam}}$ that contains all the transmission coefficients such that

$$\mathbf{a}_{\mathrm{transmitted}} = \mathbf{T}_{\mathrm{ring/beam}}\mathbf{a}_{\mathrm{incident}}, \tag{33}$$

with

$$\mathbf{T}_{\mathrm{ring/beam}_{[9\times 9]}} = \begin{bmatrix} \boldsymbol{\Pi}^{(\mathrm{I})\to(\mathrm{II})} & \mathbf{B}^{(\mathrm{II})-} & \boldsymbol{\Pi}^{(\mathrm{III})\to(\mathrm{II})} \\ \mathbf{B}^{(\mathrm{I})+} & \boldsymbol{\Pi}^{(\mathrm{II})\to(\mathrm{I})} & \boldsymbol{\Pi}^{(\mathrm{III})\to(\mathrm{I})} \\ \boldsymbol{\Pi}^{(\mathrm{I})\to(\mathrm{III})} & \boldsymbol{\Pi}^{(\mathrm{II})\to(\mathrm{III})} & \mathbf{B}^{(\mathrm{III})-} \end{bmatrix}, \tag{34}$$

$$\mathbf{a}_{\mathrm{transmitted}_{[9\times 1]}} = [\mathbf{u}_r^{(\mathrm{II})+} \;\; \mathbf{u}_r^{(\mathrm{I})-} \;\; \mathbf{u}_b^{(\mathrm{III})+}]^{\mathrm{T}}$$

and

$$\mathbf{a}_{\mathrm{incident}_{[9\times 1]}} = [\mathbf{u}_r^{(\mathrm{I})+} \;\; \mathbf{u}_r^{(\mathrm{II})-} \;\; \mathbf{u}_b^{(\mathrm{III})-}]^{\mathrm{T}}.$$

Each $\mathbf{u}_{r,b}^{(j)\pm}$ is defined as in Eq. (17) and the matrices contained in $\mathbf{T}_{\mathrm{ring/beam}}$ are presented in Section 3.2.

4.2. Simplification to two beams connected at an angle

To obtain the transmission coefficients for two beams joined at an angle without rigid joint, Eqs. (24)–(32) can be used. The terms referring to ring portion (II) and the terms involving the coefficients X_i, which represent the coupling between radial and tangential displacements in a ring, are suppressed. A $[6\times 6]$ system of equations is obtained, which can be solved numerically to give the required transmission coefficients required, see Appendix A for details.

5. Cyclic symmetry simplification

If a structure possesses the same discontinuity several times, the associated transmission coefficients need only to be calculated once. If a structure presents one or more axes of symmetry, one can simplify the model by considering only one part of the structure. For this case, the axis of symmetry can be modelled using appropriate boundary conditions (sliding conditions for example) which lead to transmission coefficients at the axes of symmetry, and the ray tracing method can be

applied in the same way as described earlier. Another type of symmetry is cyclic symmetry which occurs when a rotational structure is made of repetitive sectors. In this case, there is no direct boundary coefficients that can be used to represent the symmetry. However, simplifications can be made and these are described in the following section.

5.1. Cyclic symmetry theory

The method that simplifies the analysis of cyclic symmetric (also called rotationally periodic) structures was first developed for finite element (FE) models by Thomas [21,22]. This section introduces the basis of his work and applies it to the ray tracing method. Thomas' work is an extension of the study carried out in [23] where the structures considered were infinitely long 'chains' of identical substructures. Thomas modelled rotationally periodic structures consisting of N finite identical sectors forming a closed ring. The property of periodicity can be exploited so that the analysis of one sector gives the same information as the analysis of the entire structure [22].

With axisymmetric structures, it is well known that most modes of vibration occur in degenerate orthogonal pairs (see, for example, the case of a perfect ring [24]). The reason is that, if a mode has a maximum deflection at some point on the structure, it is clearly possible, because of the axisymmetric nature of the structure, to rotate the mode shape through any angle and not change the frequency of vibration. Thomas [22] showed that a similar effect occurs for rotationally periodic structures.

Let us consider a rotationally periodic structure consisting of N identical sectors, each of which is defined using wave amplitudes. These wave amplitudes are ordered so that the ones of the first sector are followed by those of the second sector, and so on. The overall wave amplitude vector $\mathbf{a}$ can be written as

$$\mathbf{a} = \begin{bmatrix} \mathbf{a}^{(1)} \\ \mathbf{a}^{(2)} \\ \mathbf{a}^{(3)} \\ \cdots \\ \mathbf{a}^{(N)} \end{bmatrix}, \tag{35}$$

where $\mathbf{a}^{(j)}$ is a vector containing the wave amplitudes associated with the jth sector. The sector numbers are increasing in the trigonometric direction of rotation (anticlockwise).

Thomas [22] proved that the deflections on any one sector can be written in terms of the deflections on any other, as follows:

$$\mathbf{a}^{(j)} = \mathrm{e}^{-\mathrm{i}\psi}\mathbf{a}^{(j+1)}, \quad \mathbf{a}^{(j+1)} = \mathrm{e}^{\mathrm{i}\psi}\mathbf{a}^{(j)}, \tag{36}$$

where ψ is a change of phase having the form:

$$\psi = \frac{2\pi}{N}\kappa. \tag{37}$$

In this equation, κ (an integer) is the cyclic symmetry mode number and indicates the number of waves around the circumference in a basic response.

To obtain all the possible modes of vibration of the structures [22], it is necessary to find the modes corresponding to the $N/2+1$ values of ψ, i.e.

$$\psi = 0, \frac{2\pi}{N}, \ldots, \frac{2\pi}{N}\left(\frac{N}{2}-1\right), \pi \quad \text{or} \quad \kappa = 0,1,\ldots,\frac{N}{2}-1,\frac{N}{2} \tag{38}$$

for N even, and the $(N+1)/2$ values of ψ, i.e.

$$\psi = 0, \frac{2\pi}{N}, \ldots, \frac{2\pi}{N}\left(\frac{N-1}{2}\right) \quad \text{or} \quad \kappa = 0,1,\ldots,\frac{N-1}{2} \tag{39}$$

for N odd. Each κ value corresponds to a κ- fold symmetric mode and needs to be examined. In the following section, the rotationally periodic properties are applied in the ray tracing method.

5.2. First simplification

An entire structure is analysed by considering a single 'principal' sector, as illustrated in Fig. 5(a). Artificial boundaries are introduced to model the cyclic symmetry condition. This is achieved by introducing wave amplitudes at boundaries A and B. In addition, wave amplitudes within the substructure Λ are considered.

The ray tracing method presented in Section 3 uses traditional transmission coefficients to link the waves in different parts of the system together. If only one sector is modelled, there is no physical or geometrical link between boundaries A and B as they are not in direct contact. The only property that can be used is the phase change between one end and the other (see Section 5.1). This change of phase can be considered as a 'transmission coefficient' from one end to the other, so a wave incident at one end will be 'linked' to the other end by a change of phase coefficient.

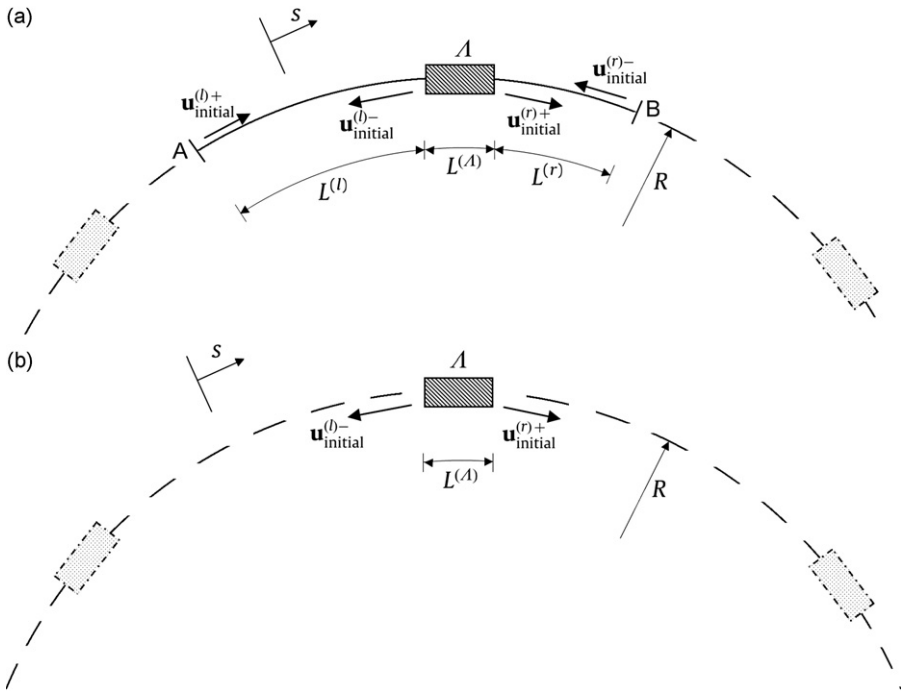

Fig. 5. (a) First simplification that involves four sets of wave amplitudes, (b) further simplification with only two sets of wave amplitudes.

If the complex-valued displacement at A is u_{A}, then, from the rotationally periodic structure properties explained in Section 5.1, the displacement at B will be u_{B} such that $u_{\mathsf{B}} = u_{\mathsf{A}} \mathrm{e}^{-\mathrm{i}(2\pi/N)\kappa}$ (or $u_{\mathsf{A}} = u_{\mathsf{B}} \mathrm{e}^{\mathrm{i}(2\pi/N)\kappa}$). As the displacements are defined entirely using wave amplitudes, it follows that the waves created at A and incident on B will have an amplitude ratio of $\mathrm{e}^{\mathrm{i}(2\pi/N)\kappa}$; while the waves created at B and incident on A will have an amplitude ratio of $\mathrm{e}^{-\mathrm{i}(2\pi/N)\kappa}$.

To apply the ray tracing method, consider an initial set of wave amplitudes $\mathbf{a}_0$, illustrated in Fig. 5(a), such that

$$\mathbf{a}_{0_{[12\times1]}} = [\mathbf{u}^{(l)+}_{\text{initial}} \;\; \mathbf{u}^{(l)-}_{\text{initial}} \;\; \mathbf{u}^{(r)+}_{\text{initial}} \;\; \mathbf{u}^{(r)-}_{\text{initial}}]^{\mathrm{T}}. \tag{40}$$

Each wave travels along its corresponding waveguide. The waves starting on the left hand side of the substructure or on the left boundary A will travel along $L^{(l)}$ and the ones on the right hand side will travel along $L^{(r)}$. In this situation the dispersion matrix $\mathbf{D}$ is given by

$$\mathbf{D}_{[12\times12]} = \begin{bmatrix} \boldsymbol{\Delta}_{L^{(l)}} & \mathbf{0} & \mathbf{0} & \mathbf{0} \\ \mathbf{0} & \boldsymbol{\Delta}_{L^{(l)}} & \mathbf{0} & \mathbf{0} \\ \mathbf{0} & \mathbf{0} & \boldsymbol{\Delta}_{L^{(r)}} & \mathbf{0} \\ \mathbf{0} & \mathbf{0} & \mathbf{0} & \boldsymbol{\Delta}_{L^{(r)}} \end{bmatrix}, \tag{41}$$

where

$$\boldsymbol{\Delta}_{L^{(j)}} = \begin{bmatrix} \mathrm{e}^{-\mathrm{i}k_1 L^{(j)}} & 0 & 0 \\ 0 & \mathrm{e}^{-\mathrm{i}k_2 L^{(j)}} & 0 \\ 0 & 0 & \mathrm{e}^{-\mathrm{i}k_3 L^{(j)}} \end{bmatrix}, \quad j = l, r.$$

The link between the left and right boundaries are given by the transmission coefficient matrix $\mathbf{T}$:

$$\mathbf{T}_{[12\times12]} = \begin{bmatrix} \mathbf{0} & \mathbf{0} & \boldsymbol{\Upsilon}^{+} & \mathbf{0} \\ \mathbf{B}^{(l)+} & \mathbf{0} & \mathbf{0} & \boldsymbol{\Pi}^{(r)\to(l)} \\ \boldsymbol{\Pi}^{(l)\to(r)} & \mathbf{0} & \mathbf{0} & \mathbf{B}^{(r)-} \\ \mathbf{0} & \boldsymbol{\Upsilon}^{-} & \mathbf{0} & \mathbf{0} \end{bmatrix}, \tag{42}$$

where $\mathbf{B}^{(l)+}_{[3\times3]}$ and $\mathbf{B}^{(r)-}_{[3\times3]}$ contain the reflection coefficients at the discontinuity Λ on its left and right hand sides, respectively; $\boldsymbol{\Pi}^{(l)\to(r)}_{[3\times3]}$ and $\boldsymbol{\Pi}^{(r)\to(l)}_{[3\times3]}$ contain the transmission coefficients from waves incident from the left side to the right side (or from the right side to the left side, respectively). The matrices $\boldsymbol{\Upsilon}^{+}$ and $\boldsymbol{\Upsilon}^{-}$ represent the change of phase

phenomenon between the cyclic symmetry boundaries in the positive s direction and negative s direction, respectively. These are given by

$$\boldsymbol{\Upsilon}^{+}=\begin{bmatrix} e^{i(2\pi/N)\kappa} & 0 & 0 \\ 0 & e^{i(2\pi/N)\kappa} & 0 \\ 0 & 0 & e^{i(2\pi/N)\kappa} \end{bmatrix}, \quad \boldsymbol{\Upsilon}^{-}=\begin{bmatrix} e^{-i(2\pi/N)\kappa} & 0 & 0 \\ 0 & e^{-i(2\pi/N)\kappa} & 0 \\ 0 & 0 & e^{-i(2\pi/N)\kappa} \end{bmatrix}. \tag{43}$$

Solving Eq. (12) with the **T** and **D** matrices defined by Eqs. (41) and (42) for all κ values (see Section 5.1); all of the natural frequencies of the entire structure can be obtained by modelling only one of its sectors.

The advantage of modelling only one sector is that the total number of unknowns is reduced. If the substructure Λ itself contains n unknowns, then the total number of unknowns in the simplified system is n+12. By comparing this number with the total number of unknowns in the non-simplified system (n+6)N, it is clear that taking into account cyclic symmetry greatly simplifies the analysis and reduces the computation time.

5.3. Further simplification

The previous section introduced artificial boundaries to take account of cyclic symmetry. The change of phase from one end of a sector to the other end is expressed in the transmission matrix, where waves incident on symmetry boundaries are not reflected but 'linked' to the other end of the sector. A further simplification can be made to the analysis, and this is presented here. For free-vibration analysis, Eq. (11) can be re-written as $\mathbf{a}=\mathbf{TDa}$. With the same structure and notation as in Section 5.2, this gives

$$\mathbf{a}=\begin{bmatrix} \mathbf{0} & \mathbf{0} & \boldsymbol{\Upsilon}^{+} & \mathbf{0} \\ \mathbf{B}^{(l)} & \mathbf{0} & \mathbf{0} & \boldsymbol{\Pi}^{(r)\to(l)} \\ \boldsymbol{\Pi}^{(l)\to(r)} & \mathbf{0} & \mathbf{0} & \mathbf{B}^{(r)} \\ \mathbf{0} & \boldsymbol{\Upsilon}^{-} & \mathbf{0} & \mathbf{0} \end{bmatrix}\begin{bmatrix} \boldsymbol{\Delta}_{L^{(l)}} & \mathbf{0} & \mathbf{0} & \mathbf{0} \\ \mathbf{0} & \boldsymbol{\Delta}_{L^{(l)}} & \mathbf{0} & \mathbf{0} \\ \mathbf{0} & \mathbf{0} & \boldsymbol{\Delta}_{L^{(r)}} & \mathbf{0} \\ \mathbf{0} & \mathbf{0} & \mathbf{0} & \boldsymbol{\Delta}_{L^{(r)}} \end{bmatrix}\mathbf{a}, \tag{44}$$

where

$$\mathbf{a}=[\mathbf{u}^{(l)+}\ \ \mathbf{u}^{(l)-}\ \ \mathbf{u}^{(r)+}\ \ \mathbf{u}^{(r)-}]^{\mathrm{T}}. \tag{45}$$

Expanding the second and third equations of (44) and re-arranging in matrix form, it can be shown that

$$[\mathbf{u}^{(l)-}\ \ \mathbf{u}^{(r)+}]^{\mathrm{T}}=\begin{bmatrix} \boldsymbol{\Pi}^{(r)\to(l)} & \mathbf{B}^{(l)} \\ \mathbf{B}^{(r)} & \boldsymbol{\Pi}^{(l)\to(r)} \end{bmatrix}\begin{bmatrix} \boldsymbol{\Delta}_{L^{(r)}}\boldsymbol{\Upsilon}^{-}\boldsymbol{\Delta}_{L^{(l)}} & \mathbf{0} \\ \mathbf{0} & \boldsymbol{\Delta}_{L^{(l)}}\boldsymbol{\Upsilon}^{+}\boldsymbol{\Delta}_{L^{(r)}} \end{bmatrix}[\mathbf{u}^{(l)-}\ \ \mathbf{u}^{(r)+}]^{\mathrm{T}}. \tag{46}$$

Comparing this equation with Eq. (11), it can be deduced that the ray tracing method can be used to model the entire structure with $\mathbf{a}=[\mathbf{u}^{(l)-}\ \ \mathbf{u}^{(r)+}]^{\mathrm{T}}$, $\mathbf{T}=\begin{bmatrix} \boldsymbol{\Pi}^{(r)\to(l)} & \mathbf{B}^{(l)} \\ \mathbf{B}^{(r)} & \boldsymbol{\Pi}^{(l)\to(r)} \end{bmatrix}$ and $\mathbf{D}=\begin{bmatrix} \boldsymbol{\Delta}_{L^{(r)}}\boldsymbol{\Upsilon}^{-}\boldsymbol{\Delta}_{L^{(l)}} & \mathbf{0} \\ \mathbf{0} & \boldsymbol{\Delta}_{L^{(l)}}\boldsymbol{\Upsilon}^{+}\boldsymbol{\Delta}_{L^{(r)}} \end{bmatrix}$. The matrix **D** can be simplified to

$$\mathbf{D}=\begin{bmatrix} \boldsymbol{\Delta}_{L^{(l)}+L^{(r)}}\boldsymbol{\Upsilon}^{-} & \mathbf{0} \\ \mathbf{0} & \boldsymbol{\Delta}_{L^{(l)}+L^{(r)}}\boldsymbol{\Upsilon}^{+} \end{bmatrix}, \tag{47}$$

where

$$\boldsymbol{\Delta}_{L^{(l)}+L^{(r)}}\boldsymbol{\Upsilon}^{\pm}=\begin{bmatrix} e^{i(\pm(2\pi/N)\kappa-k_1L_0)} & 0 & 0 \\ 0 & e^{i(\pm(2\pi/N)\kappa-k_2L_0)} & 0 \\ 0 & 0 & e^{i(\pm(2\pi/N)\kappa-k_3L_0)} \end{bmatrix}, \tag{48}$$

with $L_0=L^{(l)}+L^{(r)}$, which represents the distance travelled along the waveguide from one substructure to its neighbour. For example, if the substructure Λ has a length $L^{(\Lambda)}$ and is placed on a ring-based system, as in Fig. 5(a), then $L_0=(2\pi/N)R-L^{(\Lambda)}$.

From the previous derivations, the system illustrated in Fig. 5(a) can be simplified to the one presented in Fig. 5(b). The influence of the cyclic boundaries appears in the dispersion matrix (Eq. (47)). The transmission coefficient matrix now contains terms on its diagonal: each wave is a function of itself (after some propagation, decay and change of phase). This simplification further reduces the number of unknown wave amplitudes: the total number of unknowns is now n+6, where n is the number of unknowns present in the substructure itself.

To obtain all of the natural frequencies of the entire structure, the simplification presented above reduces the analysis of a (n+6)N unknowns system to $N/2+1$ analyses of a system with n+6 unknowns, when N is even; or to $(N+1)/2$ analyses of a system with n+6 unknowns, when N is odd, see Section 5.1.

5.4. Obtaining the mode shape of the entire structure

Once the natural frequencies ω_n have been derived using Eq. (12), the wave amplitudes of the modelled sector (numbered 1) are obtained by solving $[\mathbf{I}-\mathbf{T}(\omega_n)\mathbf{D}(\omega_n)]\mathbf{a}_n^{(1)}=\mathbf{0}$, see Section 3. Here $\mathbf{a}_n^{(1)}$ contains the wave amplitudes defining the mode shape in the single 'principal' sector. To obtain the mode shape for the complete structure, the results

obtained for the single sector are extended using Eqs. (36) and (37). Eq. (36) is an iterative expression that gives the mode shape of sector (j+1) as a function of the mode shape of the previous sector (j) (in the anticlockwise direction). The wave amplitudes of the jth sector (j=1, 2, …, N) can also be expressed using those of the 1st sector only with the following equation derived from Eq. (36):

$$\mathbf{a}_n^{(j)} = \mathrm{e}^{\mathrm{i}(2\pi/N)\kappa(j-1)}\mathbf{a}_n^{(1)}. \tag{49}$$

From Eq. (49), the wave amplitudes in any sector of the structure can be calculated. The displacements corresponding to the mode shape can then by calculated using the wave expressions of Section 2.

6. Applications

This section presents numerical examples for a perfect ring, a ring with added masses, regular polygons and the MEMS sensor structure shown in Fig. 1. The transmission coefficients derived in Section 4 are combined with the cyclic symmetry simplification method presented in Section 5 to determine the natural frequencies and mode shapes. Results are compared with Rayleigh–Ritz and FE methods for validation purposes, but the dynamic stiffness method, alternative method that uses exact functions to model the vibration, could also have been employed to analyse this kind of network structures.

6.1. Perfect ring

It is straightforward to obtain an analytical expression for the natural frequencies of a perfect ring using the ray tracing approach. In Eq. (12), the transmission matrix **T** is set equal to the identity matrix as there are no joints to interrupt the waves travelling around the ring, and the diagonal dispersion matrix **D** contains the terms $\mathrm{e}^{-\mathrm{i}2\pi Rk_i}$ (i=1, 2, 3). Solving Eq. (12) analytically gives wavenumber solutions of the form k_n=n/R (n=0, 1, 2, …). By substituting the k_n values into the dispersion relation (which can be found in [20]) and solving, it can be shown that the natural frequencies are given by

$$\omega_n^{\pm} = \sqrt{\frac{E}{2\rho R^2}\Phi(n)\left(1 \pm \sqrt{1-\frac{\Psi(n)}{(\Phi(n))^2}}\right)}, \tag{50}$$

with n=0, 1, 2, …, $\Phi(n) = ((I/AR^2)n^2+1)(n^2+1)$ and $\Psi(n) = (4I/AR^2)n^2(n^2-1)^2$. For each value of n, two frequencies are obtained, one representing mainly extensional vibration and one representing mainly flexural vibration. These natural frequencies are identical to those given in [25], which are derived from the natural frequencies of cylindrical shells.

6.2. Perfect ring with identical uniformly spaced point masses

Consider a ring with N identical uniformly spaced point masses. Here, the ray tracing approach using the cyclic symmetry simplification requires the transmission coefficient corresponding to a single point mass. Calculation of the transmission coefficients for a ring with an attached mass can be obtained using the equations presented in Section 4.1, by considering the rigid joint to have non-zero mass, zero length and zero moment of inertia. All of the matrices needed for the natural frequency analysis are $[6\times 6]$ square matrices, and the wave amplitudes relate to extensional, flexural and decaying waves in both directions. For a particular cyclic mode number κ, the dispersion matrix will contain terms $\mathrm{e}^{-\mathrm{i}(2\pi/N)(Rk_i \pm \kappa)}$ (with i=1, 2, 3 and $\kappa = 0, 1, \ldots, N/2$ for N even or $\kappa = 0, 1, \ldots, (N-1)/2$ for N odd), see Section 5.

McWilliam et al. [26] investigated the case of identical masses distributed uniformly around the circumference of a perfect ring. They obtained simplified analytical expressions using the Rayleigh–Ritz method for the natural frequencies and also derived frequency splitting rules, which indicate that the natural frequencies will split only when $2n/N$ is an integer, n being the mode number. It is found that the natural frequencies obtained by the ray tracing method are in accordance with the natural frequency splitting rules of [26]. The frequencies of the flexural modes are illustrated in Table 1 for different combinations of n (=2, 3, …, 6) and N (=0, 1, …4). For the N=0, 1, 2 and N=4 cases (not N=3), the angular position of the masses does not change as uniformly spaced masses are added. For any n, the corresponding natural frequencies decrease. However, changing the angular position of masses on the ring changes the mass distribution and can either increase or decrease the natural frequency, e.g. see N=2, 3. Both analyses show very good agreement for the frequency split. However, the frequencies calculated with the two methods differ slightly due to the consideration of Poisson's ratio in Flügge's strain–displacement relations used to calculate the natural frequency of the original perfect ring (with N=0) in [26]. Poisson's ratio is not taken into account in the present ray tracing approach as shear deformation is neglected.

6.3. Regular polygons

Let us consider in-plane vibrations of regular polygons having N sides and with each corner a distance R from the centre. For such polygon, the external angle α between two sides is $\alpha = 2\pi/N$ and the length L_0 of one side is $L_0 = 2R\sin\alpha/2$, see Fig. 6.

Table 1
Natural frequencies (Hz) splitting of the flexural modes for a perfect ring with identical uniformly spaced mass for various combinations of mode and added masses, calculated with the ray tracing method or with expressions given in [26].

	N=0		N=1		N=2		N=3		N=4	
	Ray tr.	[26]	Ray tr.	[26]	Ray tr.	[26]	Ray tr.	[26]	Ray tr.	[26]
n=2	35.1	36.8	34.7	36.4	34.3	36.0	34.4	36.0	33.7	35.3
	–	–	35.0	36.7	34.9	36.6	–	–	34.7	36.4
n=3	99.2	104.0	98.1	102.8	96.9	101.6	95.8	100.4	96.7	101.3
	–	–	99.1	103.9	99.0	103.7	98.8	103.6	–	–
n=4	190.3	199.5	188.0	197.0	185.7	194.6	186.6	195.5	181.2	190.0
	–	–	190.1	199.3	189.0	199.1	–	–	189.7	198.8
n=5	307.7	322.6	304.0	318.5	300.4	314.5	302.1	316.2	300.1	314.2
	–	–	307.5	322.4	307.4	322.2	–	–	–	–
n=6	451.4	473.2	446.0	467.1	440.7	461.2	435.3	455.6	430.7	450.1
	–	–	451.2	473.0	451.1	472.9	450.9	472.7	450.7	472.5

With R=0.3 m, radial thickness=0.005 m, axial length=0.1 m. The material used is steel, with $\rho = 7850\,\mathrm{kg/m^3}$, $E = 206 \times 10^9\,\mathrm{N/m^2}$ and Poisson's ratio=0.3. Each additional point mass has a mass of 0.1 kg.

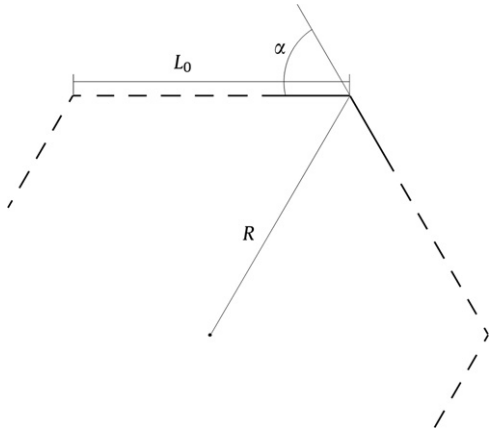

Fig. 6. Regular polygon with N sides.

In order to apply the ray tracing method, the transmission coefficients of one corner are calculated using the analysis presented in Section 4.2. The use of the cyclic symmetry simplification greatly reduces the number of unknowns, especially for large N. For any N, only six waves are required (extensional, flexural and decaying). Natural frequencies calculated for different values of N and κ are compared with results from an FE analysis using Euler/Bernoulli beam elements in Table 2. The natural frequencies found using the two methods are in perfect agreement up to five significant figures.

These analyses were performed for a fixed distance R between the centre and one corner and only the number of sides was changed. When the number of sides tends to infinity, it is expected that the natural frequencies of the polygon should tend to those of a perfect ring with radius R. This behaviour is illustrated in Fig. 7 where the natural frequencies for $\kappa = 2$ and 3 tend to the corresponding perfect ring natural frequencies ω_2 and ω_3 for flexural modes, which can be calculated using Eq. (50) and are given in Table 1 (with N=0 and n=2, 3).

6.4. Ring-based rate sensor

The ring-based rate sensor presented in Figs. 1 and 8 was modelled using the cyclic symmetry simplification. The dimensions used are given in Fig. 8(b). Only a single leg (three beam portions) is modelled. The ring is taken into account using the analysis presented in Section 5.3, i.e. waves impinging and leaving the discontinuity ring/leg are still considered. Eight identical sectors are required to complete the entire structure (N=8). It is assumed that the leg and ring are connected at a single point (only the centreline is modelled). The transmission coefficients for the different joints are calculated using the analysis presented in Section 4.

Table 2
Natural frequencies (Hz) for regular polygons with N sides calculated with the ray tracing method and a FE model (100 two-dimensional Euler/Bernoulli beams elements per side).

	N=3		N=4		N=5		N=6	
	Ray tr.	FE	Ray tr.	FE	Ray tr.	FE	Ray tr.	FE
$\kappa=0$	97.503	97.503	146.20	146.20	211.39	211.39	291.66	291.66
	205.84	205.84	280.16	280.16	391.69	391.69	532.57	532.57
	526.62	526.62	788.18	788.18	1134.9	1134.9	1553.1	1553.1
$\kappa=1$	70.415	70.415	126.87	126.87	203.51	203.51	299.48	299.48
	240.59	240.59	327.30	327.30	445.21	445.21	590.31	590.31
	441.31	441.31	34.353	34.353	1078.4	1078.4	1526.1	1526.1
$\kappa=2$	–	–	37.131	37.131	41.773	41.773	39.982	39.982
	–	–	64.517	64.517	123.33	123.33	213.60	213.60
	–	–	443.69	443.69	618.81	618.81	794.51	794.51
$\kappa=3$	–	–	–	–	–	–	99.841	99.841
	–	–	–	–	–	–	129.04	129.04
	–	–	–	–	–	–	973.34	973.34

Dimensions and material properties are the same as those given in Table 1.

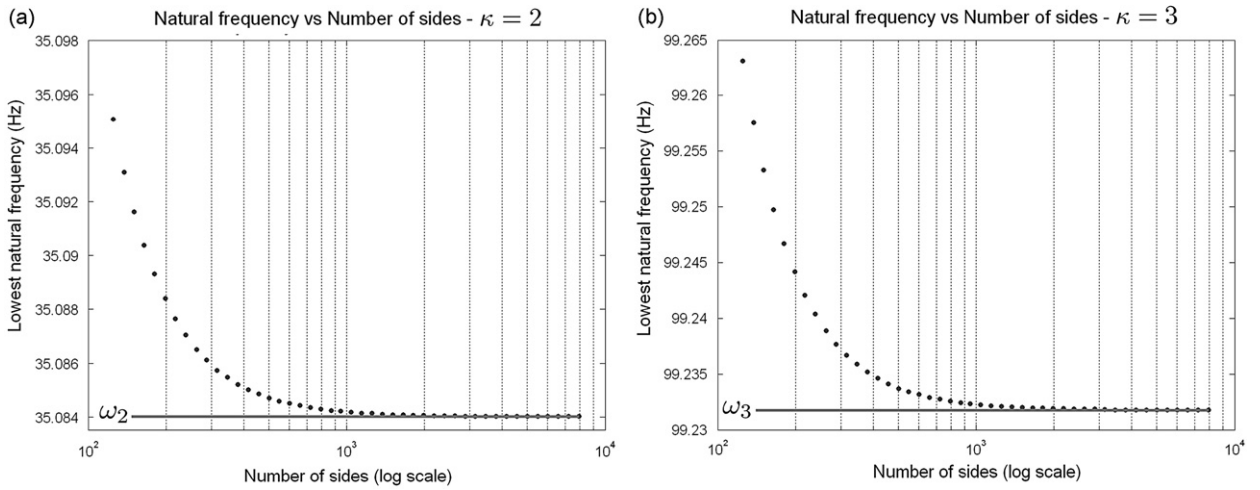

Fig. 7. Lowest natural frequency calculated with the ray tracing method of a regular polygon with $\kappa=2$ (a) or $\kappa=3$ (b), function of its number of sides N. The same dimensions and material properties as those in Table 1 are used. ω_2 and ω_3 are the n=2 and 3 natural frequencies for flexural modes in a perfect ring, see Eq. (50).

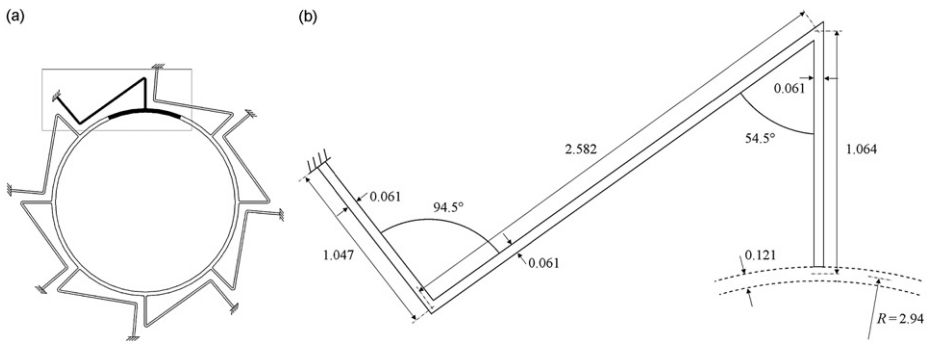

Fig. 8. (a) Ring-based rate sensor with cyclic symmetry and its 45° principal sector; (b) actual modelled structure and its dimensions in mm (with axial thickness = 0.1 mm).

Table 3
Natural frequencies (Hz) for the ring-based rate sensor calculated with the ray tracing method and an FE model (two-dimensional Euler/Bernoulli beams elements and two-dimensional Timoshenko beams elements, with 0.85 as shear correction factor, of approximate length 0.01 mm).

	Ray tracing	FE analysis		Diff. (%)
		Euler beams	Timoshenko beams	
$\kappa=0$	18533	18533	18479	0.29
	40894	40894	40832	0.15
	67511	67511	67215	0.44
$\kappa=1$	11958	11958	11925	0.28
	38676	38676	38612	0.16
	66157	66157	65880	0.42
$\kappa=2$	14269	14269	14253	0.12
	38079	38079	38013	0.17
	65702	65702	65433	0.41
$\kappa=3$	32263	32264	32205	0.18
	41229	41229	41130	0.24
	66310	66310	66043	0.40
$\kappa=4$	35884	35884	35828	0.15
	55281	55281	55056	0.41
	73231	73231	72949	0.39

The ring dimensions are presented in Fig. 8(b). The material used is silicon whose properties are $\rho=2329\,\mathrm{kg/m^3}$, $E=170\times10^9\,\mathrm{N/m^2}$ and Poisson's ratio is taken =0.28.

Using the ray tracing method with cyclic symmetry simplification, the wave amplitude vector contains 24 unknowns (six waves per beam section and six waves leaving the discontinuity ring/leg along the ring). To obtain all of the natural frequencies of the ring-based rate sensors, five different analyses ($\kappa=0, 1, 2, 3, 4$, see Section 5) are performed. The calculated frequencies are compared with FE predictions using Euler/Bernoulli and Timoshenko two-dimensional beam elements in Table 3. As in the case of regular polygons (Section 6.3), the converged FE solution gives natural frequencies that agree to five significant figures with the ray tracing model when Euler/Bernoulli elements are used, see Table 3. With Timoshenko elements, the percentage differences are less than 0.5 percent. This difference is due to the shear deformation being neglected, and it can be seen that the difference generally increases as the mode number increases, as expected.

The numerical solution times of the two methods are similar as the number of elements employed in the FE analysis to model an eighth of the ring-based rate sensor is relatively small. However, the matrices involved in the ray tracing approach are much smaller, because, similarly to the dynamic stiffness approach, only a single 'element' is used to model an entire component of the combined system (one beam, one ring portion, etc.).

From the cyclic symmetry of the system, it can be shown [22] that two orthogonal modes exist for every $\kappa=1, 2, 3$, while the $\kappa=0, 4$ modes are unique. Fig. 9 presents the mode shape (and its orthogonal complement) for the two lowest natural frequencies of $\kappa=0, 1, 2, 3, 4$. The displayed mode shapes were obtained using the ray tracing method and are similar to those given by the FE analysis. For interpretation, the first mode shape with $\kappa=0$ corresponds to rigid body mode of a free ring rotating about its centre, while the first mode shape with $\kappa=1$ corresponds to rigid body translation of a free ring. The first mode shapes with $\kappa=2$ and 3 represent the operating modes (and their orthogonal companion) of the sensor. In these modes, the flexural vibrations of the ring are maximum (compared to the legs vibrations) and easy to pick up accurately in practise by inductive means. The vibrating parts in the higher order modes are mainly the legs and those are not relevant for practical sensing. The main conclusion of this study is that, subject to the assumptions that shear deformation and rotary inertia are neglected and by modelling the centreline of the ring only (two-dimensional Euler/Bernoulli beam elements), the results obtained using the ray tracing method are in excellent agreement, for low and higher order modes, with those obtained using the FE method but with greatly reduced computational effort.

7. Summary and conclusion

In this paper, a systematic approach based on wave propagation and Euler–Bernoulli beam theory is presented to study the free vibration of ring/beams structures. This ray tracing method has been found to yield accurate predictions for the natural frequencies and mode shapes of waveguide structures such as a ring-based rate sensor system. The wave motions at the discontinuities are described by the transmission coefficient matrices, which include the effects of decaying wave components. The proposed wave approach is exact, and with the availability of propagation and transmission matrices, the vibration analysis is systematic and concise. The transmission matrices were derived from displacement continuities and

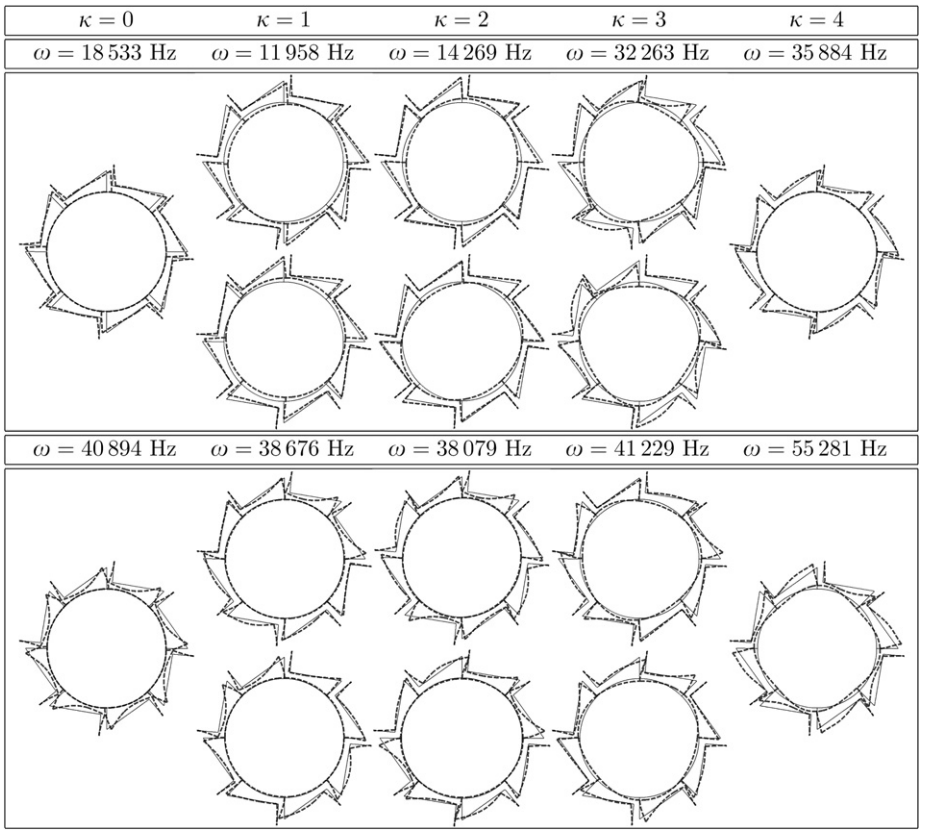

Fig. 9. Mode shapes of the ring-based rate sensor for the two lowest natural frequencies of each value of κ.

force equilibrium conditions at the discontinuity. A cyclic symmetry simplification, based on the fact that the displacement in one sector is related to the displacement in a neighbouring sector, greatly reduces the complexity of the analysis. This vibration analysis is found to be very efficient compared to FE methods which are computationally expensive if different meshes need to be generated. The method presented is illustrated for various examples.

In subsequent papers, the interaction of the resonator with its support will be assessed. The wave approach presented here is an efficient way to model the vibrational energy flow from the resonator towards its support. Using the ray tracing method, the stress sources that are responsible for support losses, the energy stored in the resonator and the associated quality factor can be calculated easily.

The approach focuses on in-plane vibration but can be adapted easily to out-of-plane motion. For three-dimensional vibration, the motion of the ring/beam structure can be defined by a longitudinal (along the centreline) displacement, with two flexural displacements (perpendicular to the centreline in mutually orthogonal directions) and with a torsional component representing twisting of the cross-section.

Acknowledgement

The authors gratefully acknowledge the support for this work provided by Atlantic Inertial Systems.

Appendix A. Transmission coefficients derivation for two beams connected at an angle

For two beams connected at an angle, the transmission coefficients are found by solving the following force and displacement continuity equations—these are simplifications of Eqs. (24)–(32):

$$u_b^{(\mathrm{I})} = u_b^{(\mathrm{II})}\cos\alpha - w_b^{(\mathrm{II})}\sin\alpha, \quad w_b^{(\mathrm{I})} = u_b^{(\mathrm{II})}\sin\alpha + w_b^{(\mathrm{II})}\cos\alpha, \quad \frac{\partial w_b^{(\mathrm{I})}}{\partial x} = \frac{\partial w_b^{(\mathrm{II})}}{\partial x}, \tag{A.1}$$

$$T_b^{(\mathrm{I})} = T_b^{(\mathrm{II})}\cos\alpha - S_b^{(\mathrm{II})}\sin\alpha \quad S_b^{(\mathrm{I})} = T_b^{(\mathrm{II})}\sin\alpha + S_b^{(\mathrm{II})}\cos\alpha, \quad M_b^{(\mathrm{I})} = M_b^{(\mathrm{II})}. \tag{A.2}$$

The conditions give a system of six equations in six unknowns. By considering an incident set of waves $\mathbf{a}_{\text{incident}_{[6\times1]}} = [\mathbf{u}_b^{(\text{I})+}\ \mathbf{u}_b^{(\text{II})-}]^{\text{T}}$ containing an extensional wave, a propagative wave and a decaying wave travelling in the x positive direction of (I) and negative x direction of (II), and a transmitted/reflected set of waves $\mathbf{a}_{\text{created}_{[6\times1]}} = [\mathbf{u}_b^{(\text{II})+}\ \mathbf{u}_b^{(\text{I})-}]^{\text{T}}$ the equations that give the transmission coefficients matrix $\mathbf{T}_{\text{sharp angle}}$ such as $\mathbf{a}_{\text{created}} = \mathbf{T}_{\text{sharp angle}}\mathbf{a}_{\text{incident}}$ can be expressed as

$$\begin{bmatrix} \cos\alpha & -\sin\alpha & -\sin\alpha & -1 & 0 & 0 \\ \sin\alpha & \cos\alpha & \cos\alpha & 0 & -1 & -1 \\ 0 & \mathrm{i} & 1 & 0 & \mathrm{i} & 1 \\ \mathrm{i}\cos\alpha & -\mathrm{i}\sqrt{\Omega}\sin\alpha & \sqrt{\Omega}\sin\alpha & \mathrm{i} & 0 & 0 \\ \mathrm{i}\sin\alpha & \mathrm{i}\sqrt{\Omega}\cos\alpha & -\sqrt{\Omega}\cos\alpha & 0 & \mathrm{i}\sqrt{\Omega} & -\sqrt{\Omega} \\ 0 & -1 & 1 & 0 & 1 & -1 \end{bmatrix} \cdot \mathbf{T}_{\text{sharp angle}} = \begin{bmatrix} 1 & 0 & 0 & -\cos\alpha & \sin\alpha & \sin\alpha \\ 0 & 1 & 1 & -\sin\alpha & -\cos\alpha & -\cos\alpha \\ 0 & \mathrm{i} & 1 & 0 & \mathrm{i} & 1 \\ \mathrm{i} & 0 & 0 & \mathrm{i}\cos\alpha & -\mathrm{i}\sqrt{\Omega}\sin\alpha & \sqrt{\Omega}\sin\alpha \\ 0 & \mathrm{i}\sqrt{\Omega} & -\sqrt{\Omega} & \mathrm{i}\sin\alpha & \mathrm{i}\sqrt{\Omega}\cos\alpha & -\sqrt{\Omega}\cos\alpha \\ 0 & -1 & 1 & 0 & 1 & -1 \end{bmatrix}, \tag{A.3}$$

with $\Omega = \omega\sqrt{I\rho/EA}$ and $\mathbf{T}_{\text{sharp angle}} = \begin{bmatrix} \boldsymbol{\Pi}^{(\text{I})\to(\text{II})} & \mathbf{B}^{(\text{II})-} \\ \mathbf{B}^{(\text{I})+} & \boldsymbol{\Pi}^{(\text{II})\to(\text{I})} \end{bmatrix}$ (see also the corresponding notation in Section 3.2).

References

[1] C. Fell, I. Hopkin, K. Townsend, I. Sturland, A second generation silicon ring gyroscope, in: *Proceedings of the DGON Symposium on Gyro Technology*, Stuttgart, Germany, 1999, pp. 1.0–1.14.
[2] Z. Hao, A. Erbil, F. Ayazi, An analytical model for support loss in micromachined beam resonators with in-plane flexural vibrations, *Sensors and Actuators A* 109 (2003) 156–164.
[3] D.M. Photiadis, J.A. Judge, Attachment losses of high Q oscillators, *Applied Physics Letters* 85 (3) (2004) 482–484.
[4] S. Rao, *Vibration of Continuous Systems*, John Wiley and Sons, New Jersey, USA, 2007.
[5] R.K. Livesley, *Matrix Methods of Structural Analysis*, second ed., Pergamon Press, Oxford, UK, 1975.
[6] W.H. Wittrick, F.W. Williams, A general algorithm for computing natural frequencies of elastic structures, *Quarterly Journal of Mechanics and Applied Mathematics* 24 (1970) 781–791.
[7] A.K. Gupta, W.P. Howson, Exact natural frequencies of plane structures composed of slender elastic curved members, *Journal of Sound and Vibration* 175 (2) (1994) 145–157.
[8] F.W. Williams, An algorithm for exact eigenvalue calculations for rotationally periodic structures, *International Journal for Numerical Methods in Engineering* 23 (4) (1986) 609–622.
[9] L.S. Beale, M.L. Accorsi, Power flow in two- and three-dimensional frame structures, *Journal of Sound and Vibration* 185 (1995) 685–702.
[10] K.F. Graff, *Wave Motion in Elastic Solids*, Ohio State University Press, 1975.
[11] L. Cremer, M. Heckl, E.E. Ungar, *Structure-Borne Sound*, second ed., Springer-Verlag, Berlin, Germany, 1988.
[12] B.R. Mace, Power flow between two continuous one-dimensional subsystems: a wave solution, *Journal of Sound and Vibration* 154 (1992) 289–319.
[13] B.R. Mace, Power flow between two coupled beams, *Journal of Sound and Vibration* 159 (1992) 305–325.
[14] R.S. Langley, High frequency vibration of one-dimensional systems: ray tracing statistical energy analysis and vibration localisation, Private communication, 1996.
[15] G.T. Ashby, *Directional vibration conductivity in beam structures*, PhD Thesis, University of Nottingham, UK, 1998.
[16] C. Mei, B.R. Mace, Wave reflection and transmission in Timoshenko beams and wave analysis of Timoshenko beam structures, *Journal of Vibration and Acoustics, Transactions of ASME* 127 (4) (2005) 382–394.
[17] B. Kang, C.H. Riedel, C.A. Tan, Free vibration analysis of planar curved beams by wave propagation, *Journal of Sound and Vibration* 171 (2005) 695–702.
[18] D.J. Mead, Waves and modes in finite beams: application of the phase-closure principle, *Journal of Sound and Vibration* 171 (1994) 695–702.
[19] B.R. Mace, Wave reflection and transmission in beams, *Journal of Sound and Vibration* 97 (1984) 237–246.
[20] C.M. Wu, B. Lundberg, Reflection and transmission of the energy of harmonic elastic waves in a bent bar, *Journal of Sound and Vibration* 190 (4) (1996) 645–659.
[21] D.L. Thomas, Standing waves in rotationally periodic structures, *Journal of Sound and Vibration* 37 (2) (1974) 288–290.
[22] D.L. Thomas, Dynamics of rotationally periodic structures, *International Journal for Numerical Methods in Engineering* 14 (1979) 81–102.
[23] R.M. Orris, M. Petyt, A finite element study of harmonic wave propagation in periodic structures, *Journal of Sound and Vibration* 33 (2) (1974) 223–236.
[24] C.H.J. Fox, A simple theory for the analysis and correction of frequency splitting in slightly imperfect rings, *Journal of Sound and Vibration* 142 (1990) 227–243.
[25] W. Soedl, *Vibration of Shells and Plates*, Marcel Dekker Inc., New York, USA, 1981.
[26] S. McWilliam, J. Ong, C.H.J. Fox, On the statistics of natural frequency splitting for rings with random mass imperfections, *Journal of Sound and Vibration* 279 (2005) 453–470.